Unsteady Validation Metrics for CFD in a Cylinder Array

Brandon Wilson
MAE Department
Utah State University
Logan, Utah, 84322
Email: brandon.m.wilson@aggiemail.usu.edu

Jeff Harris
MAE Department
Utah State University
Logan, Utah, 84322
Email: jeff.harr@aggiemail.usu.edu

Barton Smith
MAE Department
Utah State University
Logan, Utah, 84322
Email: bsmith@engineering.usu.edu

Robert Spall
MAE Department
Utah State University
Logan, Utah, 84322
Email: spall@engineering.usu.edu

Abstract

A validation study for various CFD models of the time-varying flow through a confined bank of cylinders is presented. The geometry approximates part of the lower plenum of a high temperature reactor and is arranged with the cylinders on equilateral triangles with pitch to diameter ratio of 1.7. Time-resolved Particle Image Velocimetry (PIV) measurement coupled with time-varying pressure measurements along the facilities walls are compared to both the Unsteady Reynolds Averaged Navier Stokes (URANS) $k-\omega$ model and Detached Eddy Simulation (DES) models. Spatial (*i.e.* time-averaged bulk velocity, local velocity distributions and pressure losses) and temporal (*i.e.* dominant frequencies and correlations) validation parameters on both the local and global scale are used for validation. It is found the DES model accurately predicts frequencies present in the pressure along the walls next to the cylinders in the first and the last cylinder, yet predicts other dominant frequencies in the remaining cylinders that are not found in the experiment. As expected, the temporal behavior of the DES was generally far superior to that of the URANS model.

1 Introduction

Simulation methods, such as computational fluid dynamics (CFD), are essential tools in engineering design. In the case of nuclear safety, improved CFD models can significantly increase the understanding of failure and accident scenarios. However, relying on CFD as the primary source of safety analysis requires strict validation of the codes and models. The importance of numerical model validation is understood and has generated the important field of Verification and Validation (V&V).

Although much attention has been given to the time-averaged validation of CFD codes, failure and accident scenarios often involve large transients and unsteady flow, thus requiring temporal validation. Transients are easily modeled by CFD codes; however, the current practice to validate these codes is achieved through time-averaged measurements, instantaneous comparisons, and results at significant discrete times, such as the final steady state. Little consideration has been directed toward the validation of the processes involved in unsteady simulations. The purpose of this paper is to suggest metrics used to validate the temporal solutions of unsteady CFD.

This paper follows the formal definitions for V&V outlined by the DoD [1, 2]: "Validation: The process of determining the degree to which a model is an accurate representation of the real world

from the perspective of the intended uses of the model." By this definition, validation of a numerical model is appropriate only for the application of the model and is not universally applicable. Code may be validated only for the specific range in which experimental data exists, as stated by Lee and Bauer [3]. Applications dominated by unsteady and transients flows must therefore be validated using unsteady and experimental data. Validation of the numerical model cannot be accomplished from localized temporal experimental results alone; localized spatial, globally integrated spatial, and temporal metrics must also be used. This guideline of a hierarchy of experimental measurements is outlined by Oberkampf *et. al.*[4].

While the meaning of validation in the time-averaged sense is not difficult to grasp, one must consider what is to be expected from an acceptable unsteady simulation. Unsteady Reynolds Averaged Navier Stokes (URANS) simulations are based on a triple decomposition of velocity, $u = U + \hat{u} + u'(t)$, where U is a constant mean, $\hat{u}$ is a velocity varying "slowly" in time, and u' is a turbulent fluctuation. The URANS results reported here represent $U + \hat{u}(t)$. Any variation in time is, by definition, due to factors at much longer time scales than turbulence. In the experiments, the velocity u is reported. Therefore, the time variation of any flow quantity should be expected to be smaller than in an experiment. Large Eddy Simulations (LES) and Detached Eddy Simulation (DES) compute the large scale turbulent motions while modeling the smaller scales. Therefore, LES and DES results should have smaller fluctuations than an experiment, but larger than a URANS simulation. So, while it is not realistic to expect a simulation to predict fluctuations of similar magnitude to an experiment, one could hope to obtain accurate information on the frequency behavior of an experiment. In nuclear applications, such frequencies may be important examining fluid-structure interactions.

While local and global spatial quantities are often used in the validation of unsteady numerical models, validation of temporal quantities is often not addressed. This may be for many reasons: temporal data from experimental and numerical models are difficult to compare, experimental data are often time-averaged measurements, or the scale of the unsteady fluctuations may be determined to be too small [5]. However, transient and unsteady applications often contain features that may be used to assess numerical accuracy, such as frequency and phase of vortex shedding, and time-scales (such as the autocorrelation coefficient [6]).

One example of a previous unsteady validation is the thermal mixing temperature oscillations in a T-junction. Temperature fluctuations were measured and calculated using CFD by Westin *et. al.* [7]. The unsteady numerical and experimental results were compared at various locations in the T-junction by plotting these oscillations through time. However, no attempt was made to assess the model's ability to correctly predict the dominant frequencies present in the flow. Estimation of the Taylor micro scale was estimated from the autocorrelation of the LES calculation, but is not compared to the experimental work.

In the present work, unsteady validation of a CFD solution of a confined bank of cylinders is addressed. Results are obtained through experimental measurements and CFD calculations from both experimentally and numerically consistent models. Spatial quantities (time-averaged magnitudes of velocity, pressure, and bulk velocity) and temporal quantities (dominant frequencies and fluctuations in pressure, velocity, and bulk velocity) were measured and compared to solutions predicted by CFD. Validation of unsteady temporal calculations were achieved from magnitudes of the fluctuations and dominant frequencies for each quantity.

2 Description of the Experiments

2.1 Experimental Model

The experiment (used previously for steady validation experiments [8]) consists of three sections shown in Fig. 1: inlet contraction, test section, and an outlet which connects to the downstream blower. The

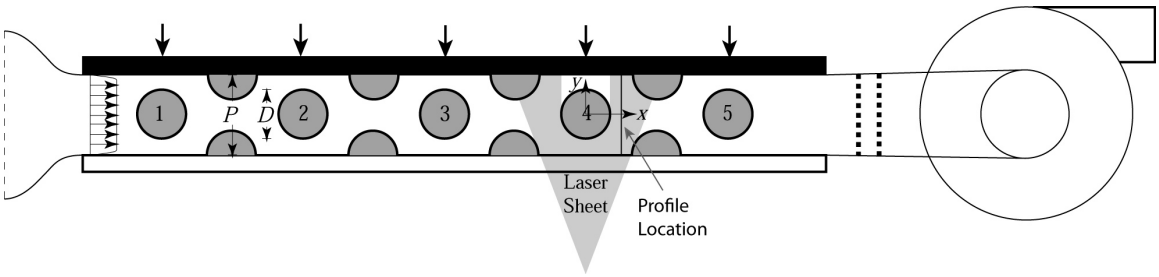

Figure 1: The test section used in this study. Air enters through screens at the left, into a contraction and into the test section. The field of view for the PIV data is shown (i.e. the laser sheet). The laser sheet moves through the near transparent side of the facility and cylinder and terminates on the opaque far side. Streamwise locations of the pressure taps are indicated with arrows on the top wall. These taps are in the spanwise center of the channel.

inlet has a 1.4:1 contraction in the span-wise direction and a 3:1 contraction in the cross-stream direction. Turbulence within the facility is controlled at the inlet by a single bank of 112 wires/cm screen. Flow leaving the test section is drawn through two perforated plates oriented perpendicular to the flow and inside the outlet. The perforated plates suppress separation and pulsations generated by the blower. The frequency-controlled centrifugal blower is located downstream of the outlet, connected to the outlet by flexible duct, and draws atmospheric air ($\rho \approx 1$ kg/m^3 in Logan) through the facility.

The test section is designed to resemble the lower plenum of a very high temperature reactor (VHTR) as shown in the schematic of Fig. 1. The test section is an $L = 89.7$ cm channel in the stream-wise (x) direction, $w = 8.53$ cm in the cross-stream (y) direction, and $H = 34.8$ cm in span-wise (z) direction. The channel contains an array of cylinders and half-cylinders ($D = 5.03$ cm) which mimic an infinite array of cylinders arranged on a equilateral triangles. Five center cylinders are placed on the cross-stream centerline with a stream-wise distance of 14.8 cm between cylinders. The fourth cylinder is made from polished polycarbonate tube, providing measurement access to the back side of the cylinder. Four sets of half-cylinders are placed directly between the centerline cylinders on the cross-stream edges. Additional details on the experimental model may be found in [8]. The dimensional flow values used in this study based on local barometric pressure are density $\rho = 1.0048 \pm 0.00325$kg/m^3, viscosity $\mu = 1.89 \times 10^{-5} \pm 1.94 \times 10^{-8}$kg/m-s and maximum bulk velocity $U_{\max} = 14.3$ m/s.

Velocity measurements were obtained using particle image velocimetry (PIV) consisting of low and high speed systems from LaVision. The low speed system consisted of a 12-bit, 1376 $\times$ 1040 pixel Imager Intense CCD camera and a New Wave dual cavity 50 mJ Nd:YAG lasers. The high speed system was composed of an 10-bit, 1024 $\times$ 1024 pixel Fastcam CMOS high speed camera and a Photonics ND:YLF 20 mJ single cavity laser. Both systems were controlled with DaVis 7.2 from LaVision [9] and seeded using oil droplets uniformly entering the test section at the inlet. Images were processed with non-deformed interrogations regions with an initial window size of 32$\times$32 and with two consecutive passes at 16$\times$16 using a 2D SCC algorithm. All interrogation regions were overlapped by 50%. Results were then post-processed using four parameters [9]: an allowable pixel range (vectors displacing more than 15 pixels are rejected), correlation peak ratio, neighboring vectors median filter, and small groups (spurious vectors in groups smaller than 5 vectors are thrown out).

Velocity measurements were made upstream and downstream of each cylinder on the $x - y$ plane (the downstream measurement plane for cylinder 3 is shown in Fig. 2). The laser sheet entered the facility from the transparent polycarbonate cross-stream side and was terminated on the far opaque side. Both the low speed and high speed lasers were located in front of the test section on a vertical traverse system and were able to be repositioned within 5μm. The cameras were mounted above the test section and were also able to repositioned vertically within 5μm using a traverse system.

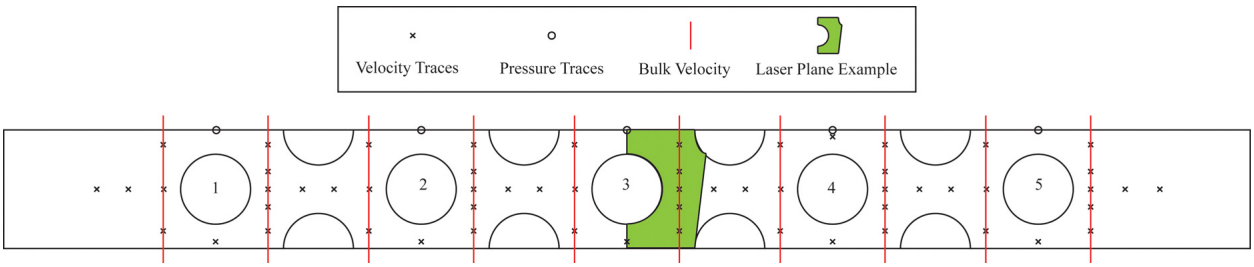

Figure 2: Numerical and experimental measurement locations. Pressure measurements and DES traces (designated by '$\circ$') were located on the upper wall on the spanwise center behind the full cylinders for both experimental and numerical data. A PIV measurement plane (denoted in green) is downstream of the fourth cylinder. Velocity trace locations are shown as '$\times$'.

Velocity time traces were extracted at specific locations from each measurement plane (shown in Fig. 2) for use as spatial and temporal validation quantities for the CFD results. Validation metrics include mean bulk and local velocities, velocity distributions, dominant frequencies, pressure-velocity and velocity-velocity spatial correlations, and autocorrelations.

Low speed measurements were obtained on $x-y$ planes at $z = 0.69D$, $1.5D$, $3.45D$, $5.4D$, and $6.21D$. At these locations, $N = 850$ images at an average rate of $f = 2.5$ Hz were used to determine the time-averaged statistics of the data. The resolution of these images were 64.5 μm/pixel. These measurements also provided reassurance that the flow was uniform through the height of the channel. Using the high speed system, ten sets of $N = 1024$ time-resolved images were obtained at $f = 1500$ Hz on the $x-y$ plane at H $= 3.64D$. These images were resolved within 88.23 μm/pixel.

Pressure taps of diameter 1.59 mm were drilled into the back wall of the facility (shown by arrows in Fig. 1). All taps were placed at the spanwise centerline and were at the same streamwise position as the axis of the full cylinders. The pressure measurements were made using five Endevco pressure transducers with a range of 1 psi and sensitivity of about 175 mV/psi. Pressure measurements were acquired using a data acquisition system from National Instruments using two approaches: first, individual measurements at 10,000 Hz for approximately 180 s and second, measurements synchronized with the high-speed PIV system at 1500 Hz.

2.2 A Note About Experimental Uncertainty

For the time-varying measurements shown in this paper, the difference between the numerical and experimental magnitudes far exceeds any experimental error. Where mean values are compared, uncertainties for the measurements have been reported in earlier work [8]. Experimental uncertainties on time (and thus frequency) are extremely small.

2.3 Numerical Model

The Reynolds-Averaged Navier Stokes standard two-equation $k-\omega$ [10] and Detached Eddy Simulation (DES) models from the general purpose CFD code FLUENT [11] were used to model the unsteady Navier-Stokes equations in the cylinder array experiment. The $k-\omega$ model was integrated to the wall. The DES model applied the SST k-ω model with low Reynolds number corrections to the unsteady Reynolds-Averaged Navier-Stokes (RANS) equations within the boundary layer. In this region, the SST k-ω based DES model utilizes a modified dissipation term for the turbulent kinetic energy (described further by Menter [11]). The filtered Navier-Stokes equations were solved using the Large Eddy Simulation (LES) model in the large unsteady turbulent scale dominant separated region.

A bounded second-order central differencing method was used to discretize the momentum terms; turbulence and dissipation terms were interpolated to the cell faces using the QUICK scheme. Pressure-velocity coupling was achieved using the SIMPLEC method. Temporal terms employed a second-order implicit time formulation. Iterative convergence for each time step was achieved by reducing the normalized residuals of all the discretized transport equation within four orders of magnitude, after which the solution advanced to the next time step. Solutions were calculated at time steps of 10^{-4} s.

The computational domain matched the experimental configuration. The mesh and geometry of the third and fourth cylinders appear in Fig. 3. The test section is composed of nine wall regions: two vertical side walls joined by four half cylinders, two horizontal walls, and five full cylinders located on the cross-stream centerline. The flow enters the numerical model at the channel inlet with uniform velocity and turbulence profiles (this model is referred to as DES steady). Perturbations from a random random fluctuating vortex field were applied to the inlet (200 vortices at the inlet) for a second DES model [11] referred to as DES perturbed. Flow exiting the numerical model leaves with the derivatives of the terms equal to zero at the outlet. The numerical model and experimental test section are dimensionally equivallent. The DES and k-ω turbulence models were applied to this three dimensional computational domain for a single mesh consisting of 3,098,000 cells with grid clustering toward the walls to ensure that $y^+ \leq 1$. The k-ω model was also applied to a coarser mesh of 1,758,250 cells to determine grid convergence.

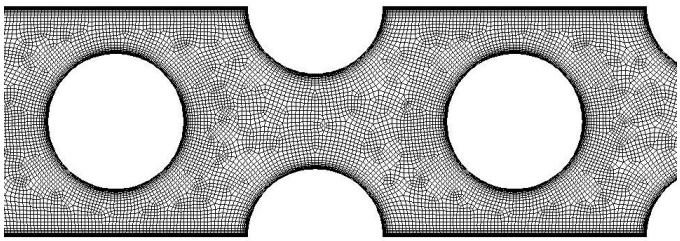

Figure 3: Computation geometry and mesh at the fourth cylinder. This mesh is repeated for the remaining cylinders.

Solutions from the above numerical model were calculated and compared to the experimental results. Validating comparisons include dominant frequencies present in the pressure and velocity signals at each cylinder and velocity distributions integrated over the time domain. Validation metrics for both the coarse and fine k-ω models are compared to determine grid convergence. Grid convergence is attained for all validation parameters presented in this paper.

3 Results and Discussion

We start our discussion of the results by examining the drag on each cylinder as predicted by unperturbed DES, since these results will illuminate the remainder of the results. Measurement of this quantity through velocity fields would require two stereo high speed PIV systems and therefore no experimental results are provided.

The drag variation with time on all five cylinders is shown in Fig. 4. Cylinders 2-5 have a similar mean drag; however, for clarity, the drag signal for cylinders 3, 4, and 5 are displaced upward by 0.5, 1.0 and 1.5, respectively. It is striking that the drag on the first cylinder (which is not displaced) is steady and significantly larger than the rest. Cylinder 2 exhibits a mean drag less than half of cylinder 1 with very large amplitude fluctuations. The largest frequency present, which is likely the shedding frequency of cylinder 1, corresponds to a Strouhal number near 0.5. A lower frequency corresponding to St = 0.25 is also clearly present. The highest frequency appears to diminish near the center of the array before reemerging at the final cylinder.

Low-speed measurements were obtained on the downstream side of the fourth cylinder at five heights described above. These measurements spanned the middle 80% of channel height and were used to determine the required blower speed to achieve the desired Reynolds number (Re = 40,000), calculate time-averaged statistics, and determine the bulk velocity. Data were acquired at three Reynolds numbers (Re = 34,000, 39,000, and 44,000) to determine the settings needed to provide Re = 40,000. Temporal fluctuations in the bulk velocity were observed in each of these measurements; however, the

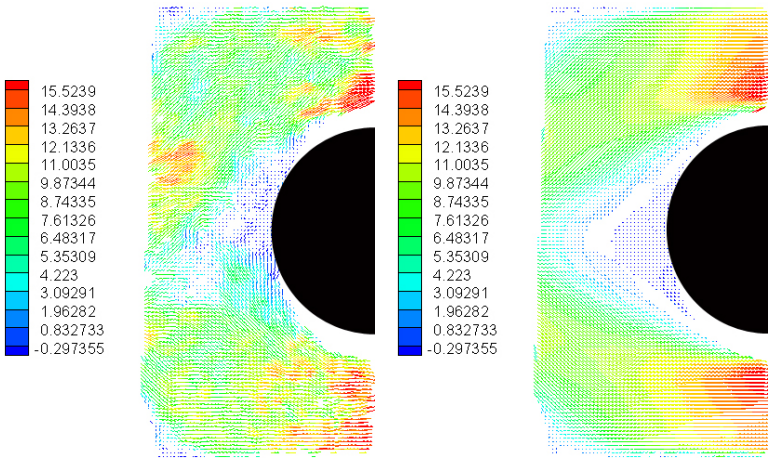

Figure 5: The instantaneous (top) and time-averaged (bottom) velocity vector fields measured by the low-speed PIV system.

standard deviation of the bulk velocity was consistent for each measurement height. The average bulk velocity at each measurement location was found to be within 2% difference of that required for Re $= 40,000$. This demonstrated that although the flow was temporally fluctuating, the time-average flow was uniform spatially at locations of the same cross-sectional area.

After determining the flow was uniform spatially, data were acquired at Re $= 40,000$ in the $x-y$ plane (see Fig. 1) using both the low and high-speed PIV systems. The low-speed data was measured at $H = 3.45D$ (instantaneous and time-averaged velocity field are shown in Fig. 5). The Reynolds number was calculated using the maximum bulk velocity ($U_{\max}$) found at the minimum cross-section) and the diameter of the cylinder (D) for the velocity and length scales, respectively.

High-speed PIV measurements were acquired on the $x-y$ plane at $H = 3.64D$. This location is about $0.2D$ lower than the centerline due to interference from the laser sheet with the pressure sensor. Laser pulses striking the far surface of the channel would produce heat waves generating highly sinusoidal noise within the pressure transducer. This noise was present while the laser was within $0.15D$ of the centerline. Therefore, high-speed measurements were acquired at the same location as the low-speed PIV measurements. A schematic of the PIV measurement planes is given in Fig. 2. Two of these high-speed measurements were oriented on the $x-y$ plane between full cylinders and the transparent wall for the second and fourth cylinders; the remaining two planes were located downstream of the fourth and fifth cylinders.

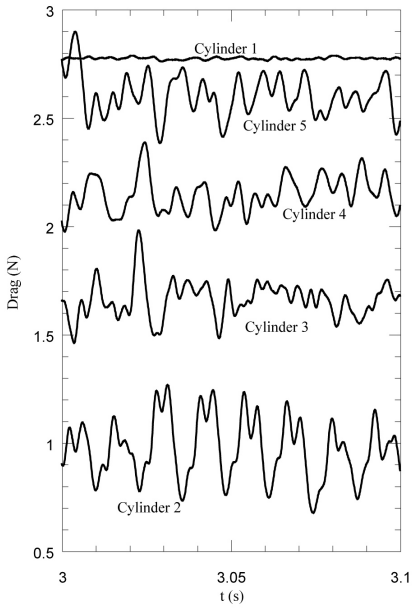

Figure 4: Temporal drag variation on the five cylinders according to DES. To improve clarity, the drag value for cylinders 3, 4, and 5 are displaced upward by 0.5, 1.0 and 1.5, respectively. The traces for cylinders 1 and 2 are not displaced.

The bulk averaged velocity on lines across the facility at several streamwise locations were computed based on the measurements. The inlet flow is steady, as expected. Quite surprisingly, large fluctuations are observed in the bulk velocity at locations downstream of cylinder 1. These fluctuations become larger until the third cylinder, after which they maintain a steady amplitude. These fluctuations indicate strong 3-D motions behind

the cylinders. Similar fluctuations are predicted by the DES models at all but the first cylinder; however, the k-ω model consistently predicts much smaller fluctuations than those seen by both the DES and experimental models.

The bulk velocity seen in both the numerical and experimental models follow a normal distribution with the standard deviations (σ) of these distributions shown in Fig. 6. The k-ω model consistently under predicts the magnitude of the bulk velocity fluctuations for all cylinder locations. Locations upstream of cylinder two are also under predicted by the DES models; however, downstream of cylinder two, the steady DES model predicts the width of the fluctuation distribution reasonably well. This is also the case at all cylinder locations but the downstream side of cylinder five for the perturbations DES model. Perturbations on the inlet velocity have very little effect on the fluctuations seen in the bulk velocity.

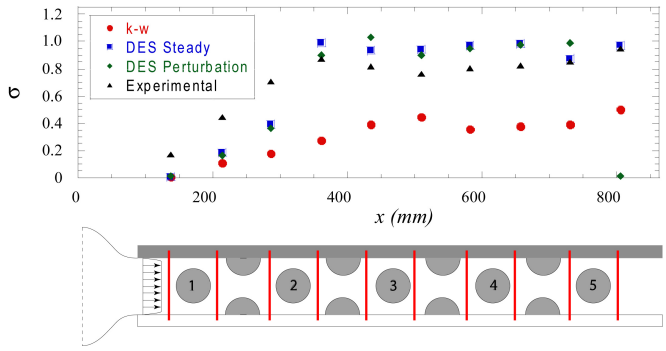

Figure 6: Standard deviation of the bulk velocity at the upstream and downstream locations for each cylinder.

Time traces for velocity and pressure point quantities were recorded during the unsteady CFD simulations. These locations (also shown as '$\circ$' in Fig. 2) consist of five pressure points along the centerline of the channel and on the opaque wall to the side of each full cylinder. Pressure and velocity measurements were measured at identical locations with the pressure transducers and extracted from the PIV results, respectively. The probability distribution function (pdf) of the experimental and numerical time traces (both URANS $k-\omega$ and DES models) for pressure on the opaque wall at each cylinder are compared in Fig. 7. Both the DES and $k-\omega$ models predict a bimodal distribution at the first cylinder. Similar results were observed by Mahon and Meskell [12]. Jet switching from side to side of the cylinder is responsible for this type of distribution. A single modal distribution is observed for all the cylinders in the experimental measurements; jet switching is never observed. The DES, $k-\omega$, and experimental models predict single mode distributions for all cylinders downstream of cylinder one. The distribution of velocity traces predict similar results and are not shown.

It is also noted that the pressure distribution widths for the experiment are similar to those from the DES, which are wider than the RANS results. Given that the RANS results contain no turbulent fluctuations, and that DES contains only large-scale fluctuations, this is to be expected.

Experimental and numerical time-traces were compared at each corresponding location to examine correlation between velocity and pressure. Note that the $t = 0$ values for the numerical and experimental results have no relation to one another since the inflow prescribed is not transient. Velocity traces downstream of cylinder four and pressure traces along the wall adjacent to cylinder four are discussed in [13]. The DES and URANS $k-\omega$ models both predict similar velocity and pressure magnitudes to the experiment; however, the $k-\omega$ model predicts more periodic fluctuations with fewer high-frequency components than observed in the experimental results. The velocity and pressure fluctuations in the steady DES and experimental models are nearly the same scale. As shown in Fig. 7, the perturbations DES model predicts much larger pressure fluctuations than the experimental model.

Since the PIV measurements are limited to 1500 Hz and $N = 1024$ velocity fields, pressure measurements were also acquired at the same frequency as the numerical time-step. The spectra of these signals for both the experimental pressure measurements and numerical pressure traces are compared in Fig. 8. At the location along side the first cylinder, the flow field lacks high frequency fluctuations and is dominated by three frequencies. The largest of these, near St = 0.5, is well predicted by both numerical models. This is the same frequency at which the drag varies and is likely the shedding frequency of the cylinder. Although the experimental results show a slightly lower frequency,

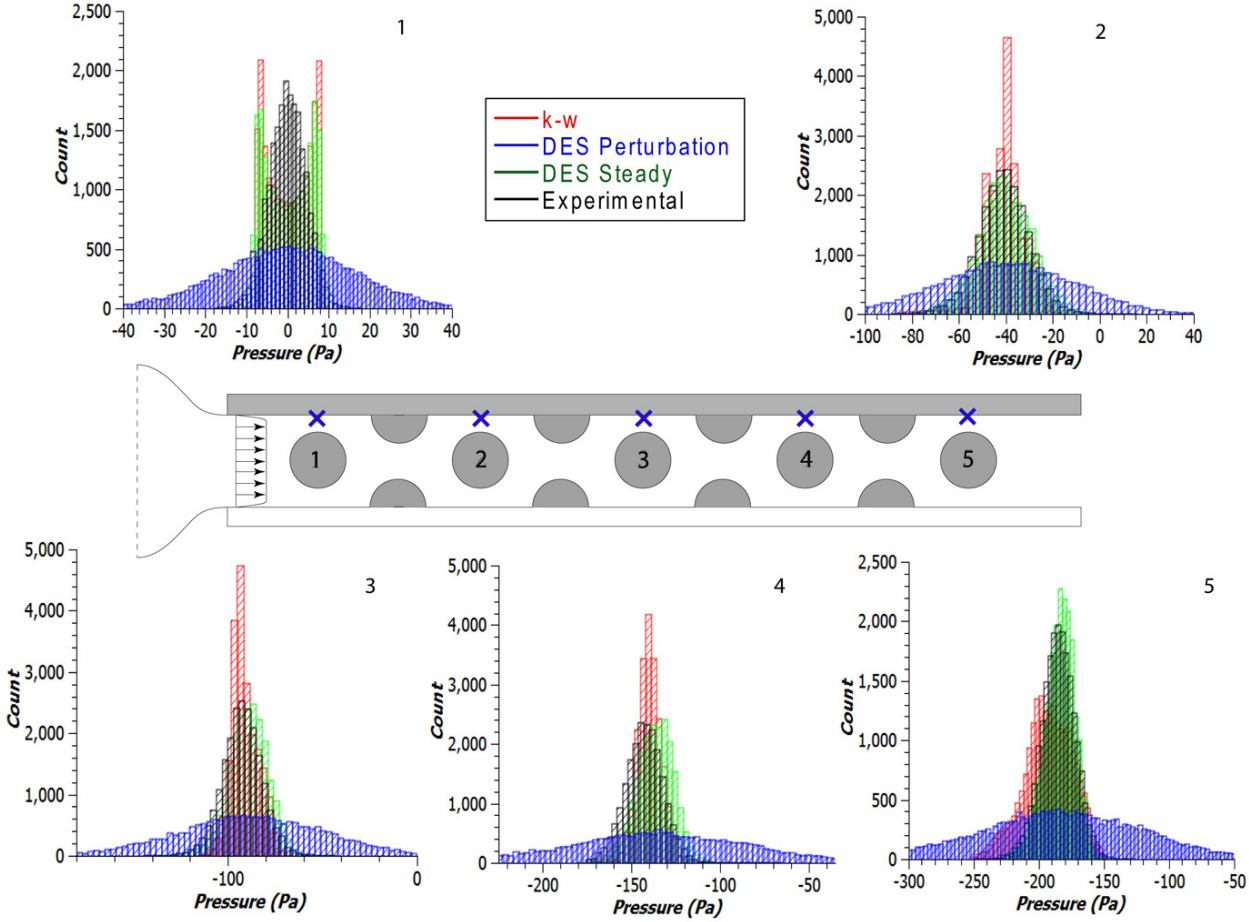

Figure 7: The distributions of pressure measured at cylinders one, two, three, and five .

the magnitude of the shedding frequency is the same for the numerical and experimental models. A second peak at double the shedding frequency is also apparent in the experiment and the numerical models, which is to be expected since pressure changes with the square of velocity. Interestingly, the DES model predicts vortex pairing as evidenced by a sub-harmonic, while the experiment has a much broader response at half the shedding frequency.

The pressure at the second cylinder in the experiment shows a very broad-band, high-frequency response with no dominant frequency. However, the numerical models each predict very large peaks at several frequencies. At the third cylinder, the DES model pressure prediction again resembles the experiment, with broad band response and no dominant frequency (although both the experiment and the model have a small peak near St = 1). The $k-\omega$ model predicts a few frequencies at the third cylinder not seen in the experiment. These frequencies are also observed in the DES model but have much smaller magnitudes. The very high frequencies in the numerical model are clearly attenuated due to the DES filter. The behavior of the experiment and the model are essentially the same for the third cylinder as the fourth. The DES model with perturbations predicts much larger broadband noise at higher Strouhal numbers than the steady DES model, with the spectral power actually increasing near the Nyquist frequency. The reason for this is under investigation.

At the fifth cylinder, both the experiment and the numerical models show a smaller shedding frequency near St = 0.2. Additionally, all the models show a smaller peak at St = 1, similar to the third cylinder.

Similar results are seen in the power spectrum for the velocity traces shown in Fig. 9. Dominant frequencies are seen primarily in the first and fifth cylinder in the experimental results. Several other frequencies are predicted by the numerical models that are not observed in the measurements. Interestingly, the power spectrum for velocity traces predicted by the perturbation DES model contains significantly less broadband noise than the pressure traces, and resembles the steady DES model.

The autocorrelation coefficient $\rho(\tau)$ [6] in time was computed for all pressure traces (cylinders one, two, three, and five are shown in Fig. 10). This coefficient is calculated as

$$\rho(\tau) = \frac{\overline{g(t)g(t')}}{\overline{g^2}}, \tag{1}$$

where $g(t)$ and $g(t')$ are a fluctuating quantity at two different times and τ is the time difference $t-t'$. The average autocorrelation coefficient in time is calculated for each measurement location and ranges from correlated ($\rho(\tau)=1$) to anti-correlated ($\rho(\tau)=-1$).

At the first cylinder, the DES and $k-\omega$ models predict similar autocorrelations with the DES model damping out slightly faster; these oscillations (which indicate periodic flow) although larger in magnitude, are similar to those seen in the experimental measurements. Perturbations added to the DES apparently help destroy the periodicity of the pressure and more closely resemble the experiment. At the second, third, and fourth cylinder, the measurement signals become and remain uncorrelated after $\tau = 0.01$s. This phenomenon is not seen at the second cylinder in any of the numerical models, as a highly periodic flow is predicted. In fact, the $k-\omega$ model predicts highly oscillatory flow ranging from correlated to anti-correlated for all cylinders. However, DES results for pressure traces at the third, fourth, and fifth cylinders predict an autocorrelation coefficient $\rho(\tau)$ smaller but much closer to the experimental results. Although both models predict much larger oscillations in the autocorrelation, the DES model predicts the experimental values much more closely than the k-ω model.

Velocity traces were also used to calculate the autocorrelation coefficient in time. The average autocorrelation in time along with measurement trace locations are shown for velocity traces downstream of each cylinder on the opaque wall side in Fig. 11. Autocorrelation results for the right and left sides of the cylinders are similar for all cases and so only the left side is shown. Although oscillations in the autocorrelation coefficient are seen in all the models at cylinder one, the magnitudes of these oscillations are over predicted by the numerical models. Similar to the pressure autocorrelation coefficient,

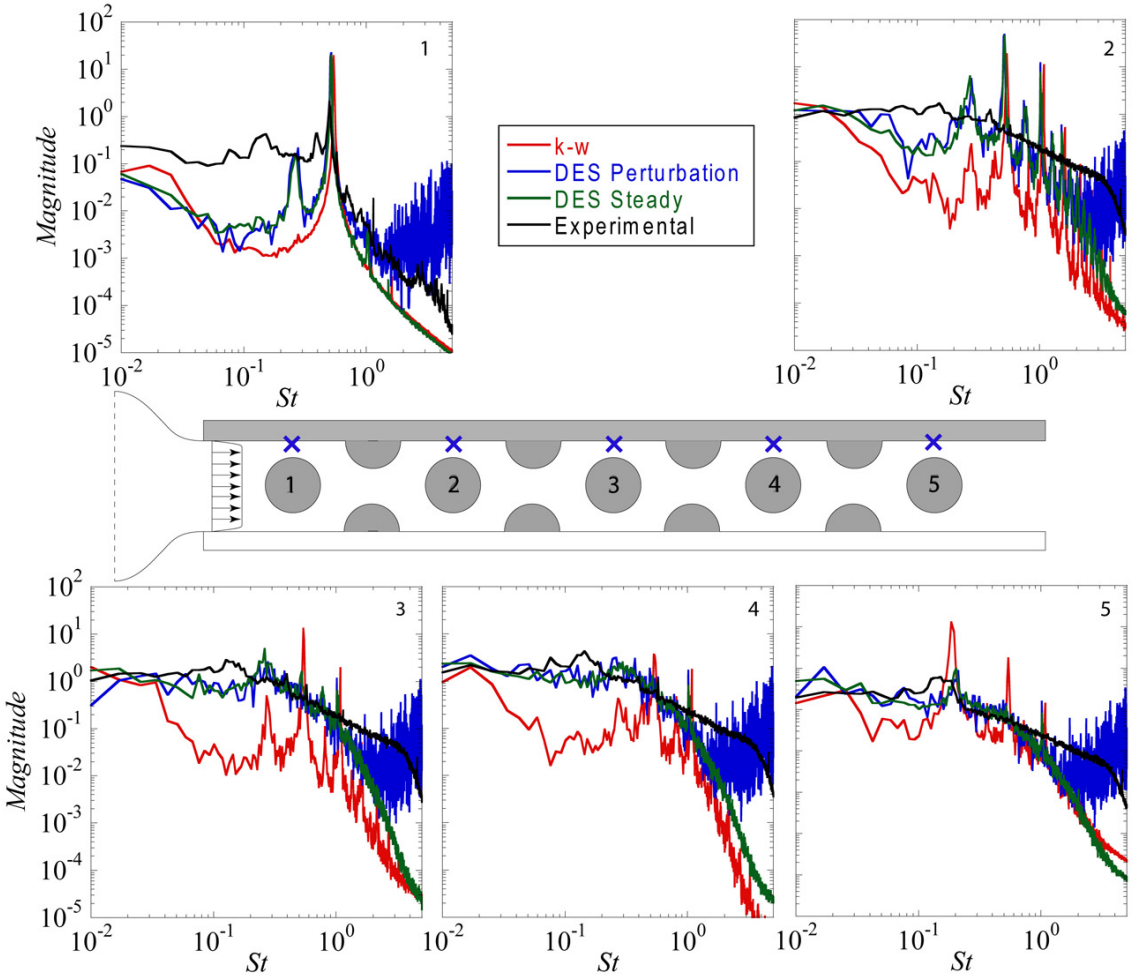

Figure 8: The power spectra for the pressure along the wall along the spanwise centerline of all five cylinders for the experimental and numerical (Steady inflow DES, DES with inflow perturbations, and k-ω) models.

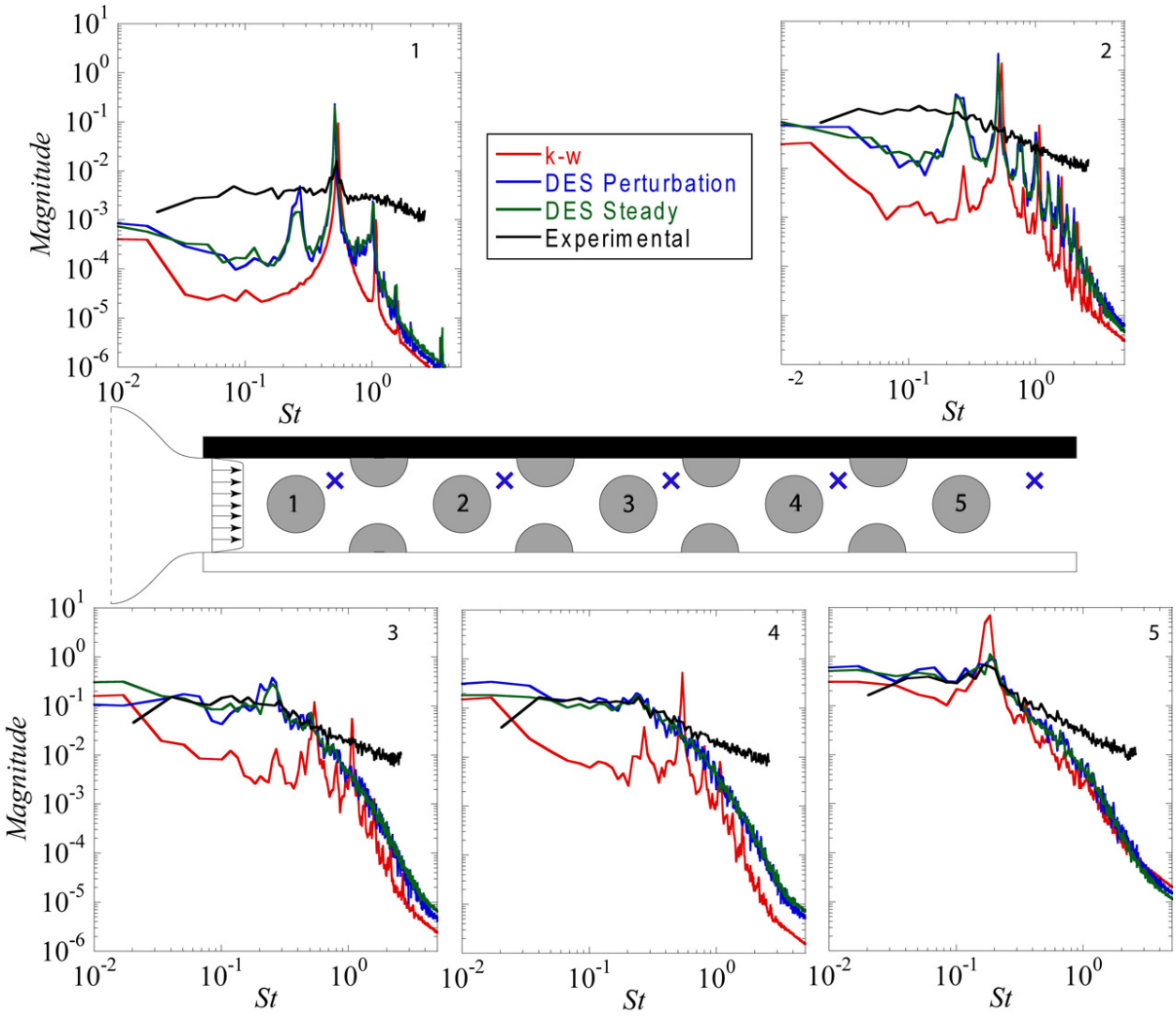

Figure 9: The average power spectra in the frequency domain for the velocity traces downstream of each cylinder on the opaque wall side for the experimental and numerical (Steady inflow DES, DES with inflow perturbations, and k-ω) models.

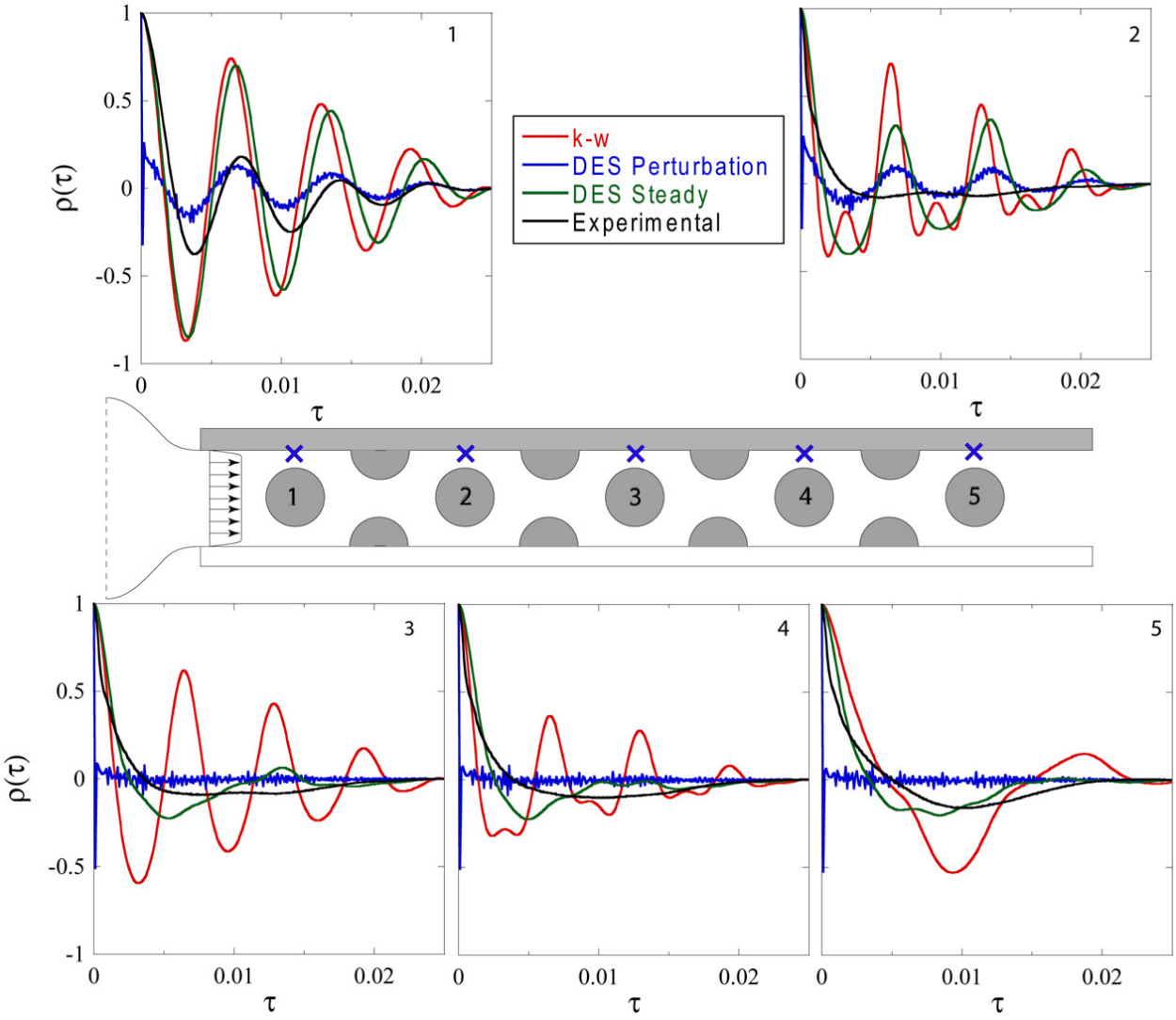

Figure 10: The average autocorrelation coefficient $\rho(\tau)$ for wall pressure along the spanwise centerline for each cylinder for the experiment and numerical models (Steady inflow DES, DES with inflow perturbations, and k-ω).

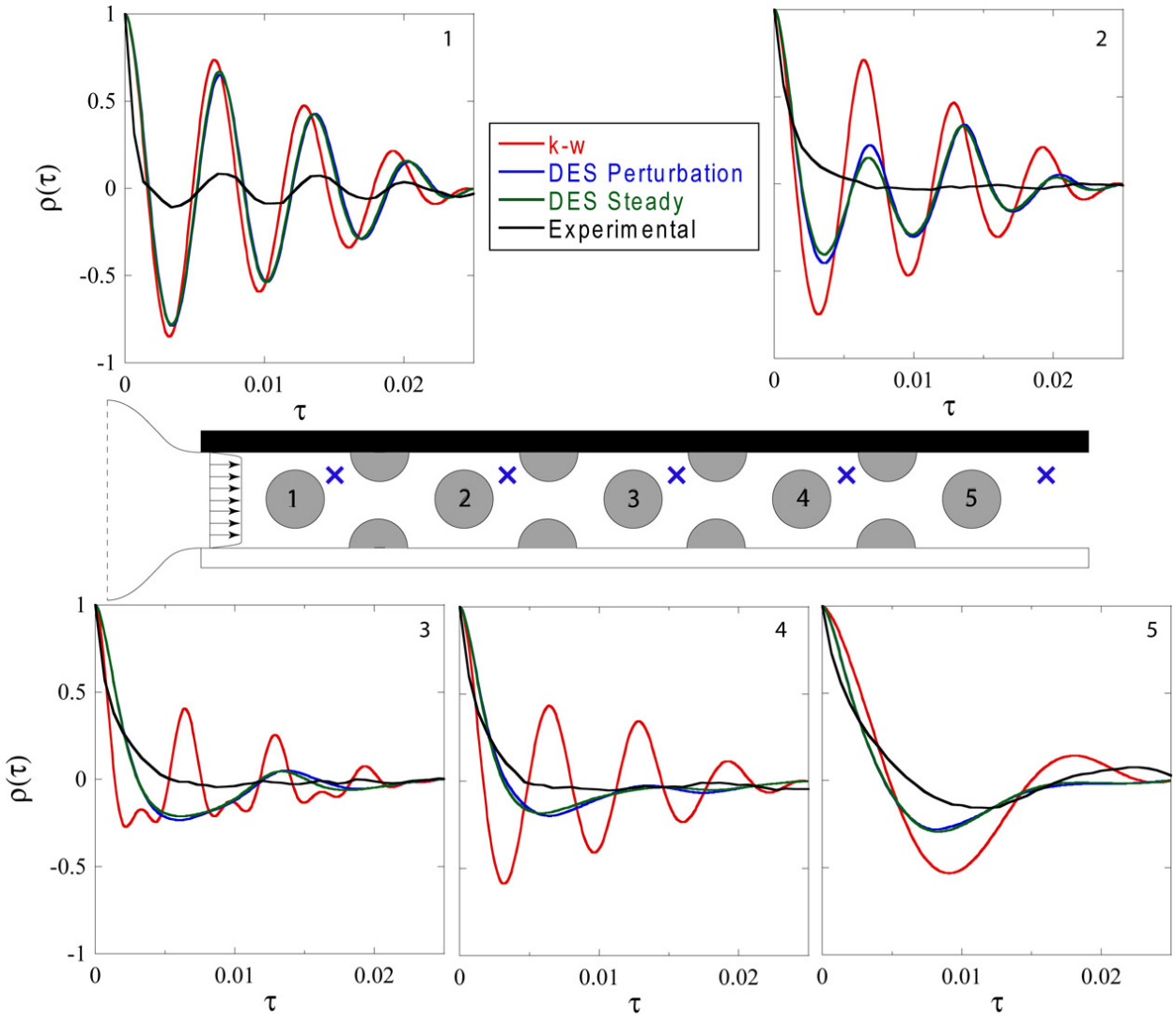

Figure 11: The average autocorrelation coefficient $\rho(\tau)$ for the velocity downstream of each cylinder near the opaque wall for the experimental and numerical (Steady inflow DES, DES with inflow perturbations, and k-ω) models.

the velocity measurement signals become uncorrelated rather quickly ($\tau \leq 0.01$s). This phenomenon is also seen in the third, fourth, and fifth cylinders of the DES solutions; however the $k-\omega$ model again predicts highly periodic velocity autocorrelation coefficients ranging from correlated to anti-correlated for all five cylinders. Oscillations are observed in the experimental autocorrelation coefficient at the fifth cylinder. Similar, yet higher frequency, oscillations are predicted by all three numerical models; however, the amplitudes of these oscillations are much smaller for the DES cases. Very little difference is seen in the steady and perturbations DES models, which is counter to the pressure autocorrelation described above.

Auto correlations were also calculated downstream of each cylinder along the lengthwise centerline in the wake region (not shown). At all locations, the experimental signal becomes uncorrelated rather quickly ($\tau \approx 0.005$s) and remains uncorrelated. As in previous locations, the $k-\omega$ model predicts highly periodic correlations. At cylinders three four and five the DES model predicts fairly uncorrelated velocities after $\tau \approx 0.015$s, similar to that seen in the experiment.

Correlation coefficients, P(τ), in time between velocity measurement pairs were also calculated as a validation metric to compare similarities mirrored on the centerline of the cylinders, such as switching, and coupled vortex shedding. This coefficient was calculated as,

$$P(\tau) = \frac{\overline{g_i(t)g_j(t')}}{\overline{g_i}\,\overline{g_j}}, \tag{2}$$

where $g_i(t)$ and $g_j(t')$ are fluctuating trace pairs at two different times and τ is once again the time difference $t - t'$.

The average correlation coefficient for five sets of velocity trace pairs are shown in Fig. 12. These trace pairs were a cylinder diameter width apart and located downstream of the cylinders next to the wake regions. Very little correlation is predicted by the measurement signals for cylinders two, three, and four; This phenomena is predicted accurately by the DES models at cylinders three and four. Oscillatory correlations between the two measurement pairs are observed at cylinders one and five for the experimental model, with a smaller frequency at cylinder 5 (as shown in the velocity spectra). While the oscillations predicted by the numerical models at these locations have similar frequencies, the amplitudes are larger in all cases except the DES models at cylinder five. At cylinder five, a reasonable representation of the correlation coefficient is predicted. The $k-\omega$ model predicts periodic correlations ranging from correlated to anti-correlated at all downstream locations.

Little or no correlation was observed upstream of the each cylinder (not shown) in the experimental measurements. This phenomena is not predicted until the third cylinder for the DES models, after which a similar correlation coefficient is predicted. The k-ω model predicts periodic correlations for all but the fifth cylinder. Once again, both DES models predict results with insignificant differences.

It is also interesting to examine time averaged global quantities, specifically the minor loss factor

$$k = \frac{\Delta p}{(0.5 n \rho U_{\max}^2)}, \tag{3}$$

where n is the number of cylinders (8 in this case). The minor loss factor for this Reynolds number is $k = 0.239$. The present DES and $k-\omega$ models predict $k = 0.243$ and $k = 0.234$ respectively, while several 2-D steady RANS model studied earlier [14] predicted values in the range $0.16 < k < 0.23$, which includes the present result.

4 Summary

A validation study has been performed on a confined bank of cylinders with special attention given to temporal validation. Experimental results are obtained using low and high speed PIV systems along with time-varying pressure measurements along the test section walls. DES and URANS simulations model the experimental model conditions as accurately as possible. Two cases for the inlet conditions (steady and vorticity perturbations) on the DES model are applied. Numerical and experimental results are compared to assess the CFD model.

Time-resolved measurements and simulated pressure and velocity signals demonstrate the ability of the DES model to predict the magnitudes of velocity and pressure fluctuations. The URANS $k-\omega$ model predicts a much more unstable (and therefore periodic) flow with smaller fluctuations. Although jet switching is predicted in all numerical models, this phenomenon is not observed in the experiment. The frequencies present due to vortex shedding and other unsteady phenomena are compared by a power spectra. Both the DES and $k-\omega$ models accurately predict frequencies present in the first and fifth cylinders; however, frequencies not present in the second through fourth cylinders of the experimental model are observed in the numerical models. Autocorrelation and correlation coefficients between velocity and pressure traces are also calculated as another validation metric. Once again, the

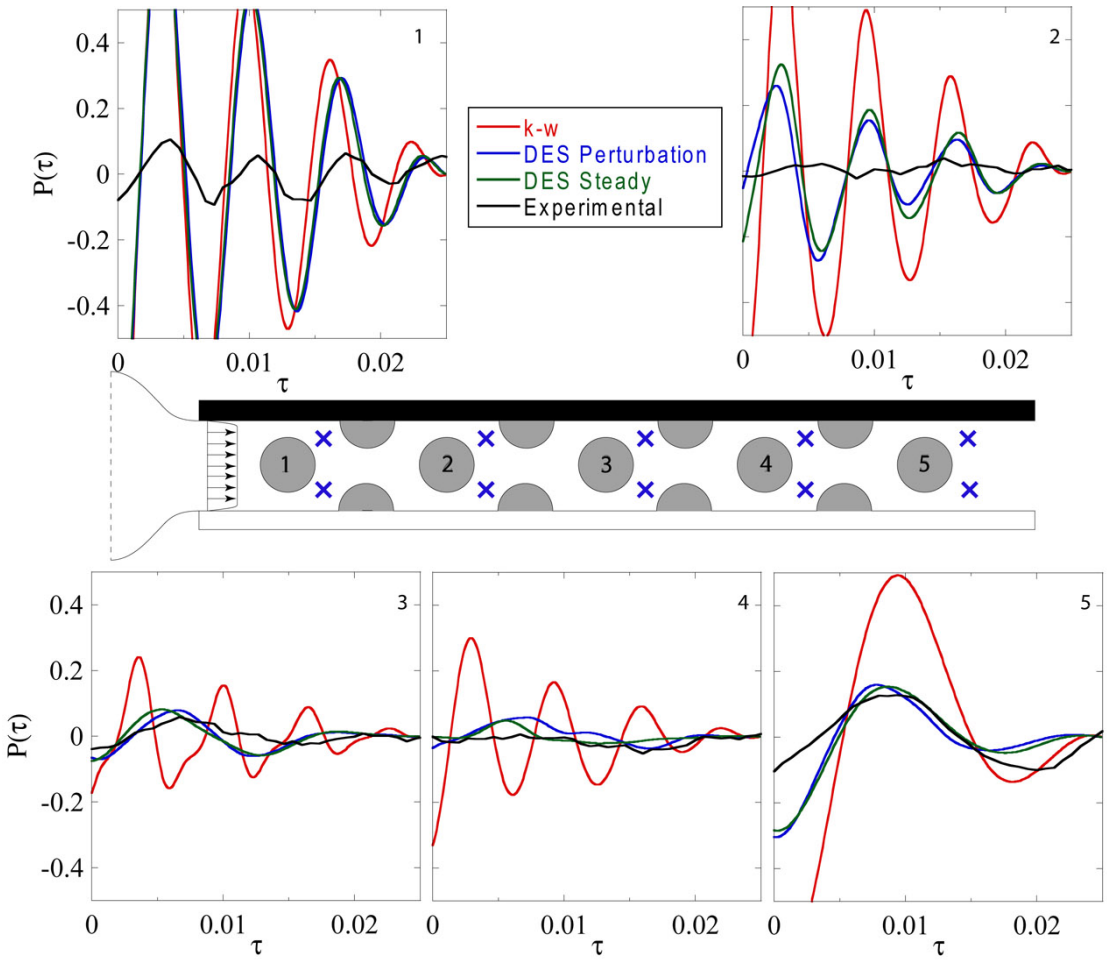

Figure 12: The average correlation coefficient (τ) for the velocity downstream of each cylinder near the walls for the experimental and numerical (Steady inflow DES, DES with inflow perturbations, and k-ω) models.

$k-\omega$ model predicts flow much more periodic and with larger time scales than the experimental model; in most cases, the DES model predicts coefficients similar to those seen in the experiment.

In spite of the surprisingly good performance of the DES numerical model to replace point behavior in velocity and pressure in several locations, we find that its prediction of a steady global parameter (the minor loss factor) to be no better than those predicted with steady RANS models.

Acknowledgment

This work has been supported by the United States Department of Energy through the Idaho National Laboratorys LDRD Project NE-156.

References

[1] DoD, 1996, DoD Instruction 5000.61: Modeling and simulation (M&S) Verification, Validation, and Accreditation (VV&A). from www.dmso.mil/docslib.

[2] DoD, 1996, Verification, Validation, and Accreditation (VV&A) Recommended practices guide. from www.dmso.mil/docslib.

[3] H. Lee and R. C. Bauer. Predictive computational fluid dynamics development and its verification and validation. In *Proceedings of ASME Fluids Engineering Division Summer Meeting*, July 2009. Paper number FEDSM2009-78147.

[4] W. L. Oberkampf and T. G. Trucano. Verication and validation in computational fluid dynamics. AIAA Fluids 2000, 2000.

[5] P. J. Roache. *Fundamentals of verification and validation*, volume 39. Hermosa publishers, 1 edition, 2009.

[6] H. Tennekes and J. L. Lumley. *A first course in turbulence*. The MIT Press, 1992.

[7] J. Westin, F. Alavyoon, L. Anderson, and P. Veber. Experiments and usteady CFD calculations of thermal mixing in a T-junction, 2007.

[8] B. L. Smith, J. J. Stepan, and D. M. McEligot. Velocity and pressure measurements along a row of confined cylinders. *J. Fluids Eng.*, 129(10):1314–1327, OCT 2007.

[9] LaVision Inc. 301 W. Michigan Ave. Suite 403, Ypsilanti, MI 48197.

[10] D. C. Wilcox. *Turbulence Modeling for CFD*. DCW Industries, Inc., 2nd edition, 1998. La Canada, Ca.

[11] Fluent 6.3. Fluent, Inc., Lebanon, NH.

[12] J. Mahon and C. Meskell. A validation database for flow in a parallel triangular heat exchanger tube array. In *American Society of Mechanical Engineers 2010 Fluids Engineering Summer Meeting*, July 2010. Paper number FEDSM2010-30298.

[13] B. Wilson, J. Harris, B. L. Smith, and R. E. Spall. Validation of unsteady cfd in a confined row of cylinders. In *Proceedings of ASME Fluids Engineering Summer Conference*, July 2010. Paper number FEDSM2010-ICNMM2010-30720.

[14] J. Hodson, R. E. Spall, and B. L. Smith. Turbulence model assessment for flow across a row of confined cylinders. *Nuclear Technology*, 161(3):268–276, 2008.